

Modeling radiation belt electron dynamics during GEM challenge intervals with the DREAM3D diffusion model

Weichao Tu,¹ G. S. Cunningham,¹ Y. Chen,¹ M. G. Henderson,¹ E. Camporeale,² and G. D. Reeves¹

Received 28 May 2013; revised 9 September 2013; accepted 10 September 2013; published 4 October 2013.

[1] As a response to the Geospace Environment Modeling (GEM) “Global Radiation Belt Modeling Challenge,” a 3D diffusion model is used to simulate the radiation belt electron dynamics during two intervals of the Combined Release and Radiation Effects Satellite (CRRES) mission, 15 August to 15 October 1990 and 1 February to 31 July 1991. The 3D diffusion model, developed as part of the Dynamic Radiation Environment Assimilation Model (DREAM) project, includes radial, pitch angle, and momentum diffusion and mixed pitch angle-momentum diffusion, which are driven by dynamic wave databases from the statistical CRRES wave data, including plasmaspheric hiss, lower-band, and upper-band chorus. By comparing the DREAM3D model outputs to the CRRES electron phase space density (PSD) data, we find that, with a data-driven boundary condition at $L_{\max} = 5.5$, the electron enhancements can generally be explained by radial diffusion, though additional local heating from chorus waves is required. Because the PSD reductions are included in the boundary condition at $L_{\max} = 5.5$, our model captures the fast electron dropouts over a large L range, producing better model performance compared to previous published results.

Plasmaspheric hiss produces electron losses inside the plasmasphere, but the model still sometimes overestimates the PSD there. Test simulations using reduced radial diffusion coefficients or increased pitch angle diffusion coefficients inside the plasmasphere suggest that better wave models and more realistic radial diffusion coefficients, both inside and outside the plasmasphere, are needed to improve the model performance. Statistically, the results show that, with the data-driven outer boundary condition, including radial diffusion and plasmaspheric hiss is sufficient to model the electrons during geomagnetically quiet times, but to best capture the radiation belt variations during active times, pitch angle and momentum diffusion from chorus waves are required.

Citation: Tu, W., G. S. Cunningham, Y. Chen, M. G. Henderson, E. Camporeale, and G. D. Reeves (2013), Modeling radiation belt electron dynamics during GEM challenge intervals with the DREAM3D diffusion model, *J. Geophys. Res. Space Physics*, 118, 6197–6211, doi:10.1002/jgra.50560.

1. Introduction

[2] The relativistic electron fluxes in Earth’s radiation belts are observed to vary greatly during geomagnetic storms and substorms [Meredith *et al.*, 2002; Reeves *et al.*, 2003; Baker and Kanekal, 2008]. Since MeV electrons can pose a significant threat to satellite electronics, there is increasing need to extensively explore and fully understand the radiation belt dynamics [Baker, 2001; Fennell *et al.*, 2001; Kessel *et al.*, 2012]. The variability of radiation belt

electrons is controlled by the competition between source and loss processes [Selesnick and Blake, 2000; Reeves *et al.*, 2003; Li, 2004; Fu *et al.*, 2011]. Radial diffusion, due to the drift-resonant interactions between radiation belt electrons and large-scale electromagnetic fields, can energize electrons by bringing them inward to stronger magnetic field regions [Hudson *et al.*, 2000; Elkington *et al.*, 2003; Li, 2004; Ukhorskiy *et al.*, 2005; Tu *et al.*, 2012]. Another important acceleration mechanism for radiation belt electrons is local heating by wave particle interactions that violate the first adiabatic invariant [Horne and Thorne, 1998; Meredith *et al.*, 2002; Horne *et al.*, 2005], for example the heating from whistler mode chorus and magnetosonic waves [Temerin *et al.*, 1994; Li *et al.*, 1997; Summers *et al.*, 1998; Horne *et al.*, 2007; Liu *et al.*, 2011]. On the other hand, wave-particle interactions can also cause the loss of radiation belt electrons by scattering them into the atmosphere. The contributing waves include chorus, considered effective outside the plasmasphere [O’Brien *et al.*, 2004; Thorne *et al.*, 2005; Shprits *et al.*, 2007], plasmaspheric hiss

¹Science and Applications Group, Los Alamos National Laboratory, Los Alamos, New Mexico, USA.

²Applied Mathematics and Plasma Physics Group, Los Alamos National Laboratory, Los Alamos, New Mexico, USA.

Corresponding author: W. Tu, Science and Applications Group, Los Alamos National Laboratory, Los Alamos, NM 87545, USA. (wtu@lanl.gov)

©2013. American Geophysical Union. All Rights Reserved.
2169-9380/13/10.1002/jgra.50560

inside the plasmasphere [Lyons *et al.*, 1972; Lyons and Thorne, 1973; Abel and Thorne, 1998; Meredith *et al.*, 2007], and electromagnetic ion cyclotron (EMIC) waves preferentially generated near the plasmapause [Fraser and Nguyen, 2001; Albert, 2003; Summers and Thorne, 2003; Loto'aniu *et al.*, 2006].

[3] One of the central questions in radiation belt research is to resolve the relative contribution of source and loss mechanisms to the enhancement and decay of radiation belt electrons. Since the observed variation is a delicate balance of the source and loss processes [Reeves *et al.*, 2003], physical models that can quantify the various processes are required. Quasi-linear theory, which applies to the interactions between charged particles and small-amplitude broadband waves, has long been used to model the resonant interactions between relativistic electrons and plasma waves [Kennel and Engelmann, 1966; Lyons, 1974a, 1974b; Summers, 2005; Albert, 2012]. Even though coherent interactions with narrowband waves and interactions with large-amplitude waves may also be important to the variations of radiation belt electrons, quasi-linear diffusion is found to be generally valid and useful for large-scale modeling of radiation belt dynamics [Albert *et al.*, 2009; Liu *et al.*, 2010; Tao *et al.*, 2012; Kim *et al.*, 2012]. Radiation belt models based on quasi-linear theory include 1D radial diffusion models [Li, 2004; Shprits *et al.*, 2005; Tu *et al.*, 2009; Chu *et al.*, 2010], 2D pitch angle and energy diffusion models [Horne *et al.*, 2005; Shprits *et al.*, 2006; Li *et al.*, 2007], and 3D diffusion models that include all three types of diffusion [Albert *et al.*, 2009; Su *et al.*, 2011; Subbotin *et al.*, 2011; Kim *et al.*, 2012]. There are also convection-diffusion models that include the dependence on drift phase [Bourdarie *et al.*, 1997; Miyoshi *et al.*, 2006; Fok *et al.*, 2008; Su *et al.*, 2010; Tu *et al.*, 2010].

[4] Our recently developed 3D diffusion model, DREAM3D, is part of the LANL DREAM (Dynamic Radiation Environment Assimilation Model) framework [Reeves *et al.*, 2012], which is described here for the first time. As a response to the “Global Radiation Belt Modeling Challenge” organized by the “Radiation Belts and Wave Modeling (RBWM)” focus group under the NSF Geospace Environment Modeling (GEM) program, in this paper we present our simulation results of the 15 August to 15 October 1990 and 1 February to 31 July 1991 periods during the Combined Release and Radiation Effects Satellite (CRRES) mission, which are defined as the training interval and challenge interval, respectively, by the RBWM focus group. The calibrated energetic electron fluxes detected by the CRRES Medium Electrons A (MEA) instrument (energy range 153 keV to 1.58 MeV) are provided by the focus group (courtesy of Bob Johnston) [Vampola *et al.*, 1992]. To apply the MEA data to our model, the electron fluxes are further converted to phase space densities (PSD) as a function of time and L^* (third adiabatic invariant [Roederer, 1970]) for fixed μ and K values (first and second adiabatic invariants). The adiabatic invariants are calculated using the Tsyganenko T89 magnetic field model [Tsyganenko, 1989] as implemented in our LANLGeoMag library. The details of our 3D diffusion model are introduced in section 2. Our simulation results are presented in section 3 followed by discussion and conclusions.

2. Model Description

[5] Our 3D diffusion model is based on the Fokker-Planck equation [Schulz and Lanzerotti, 1974]:

$$\frac{\partial f}{\partial t} = L^2 \frac{\partial}{\partial L} \left(\frac{D_{LL}}{L^2} \frac{\partial f}{\partial L} \right) + \frac{1}{p^2} \frac{\partial}{\partial p} \left(p^2 D_{pp} \frac{\partial f}{\partial p} \right) + \frac{1}{G} \frac{\partial}{\partial \alpha} \left(G D_{aa} \frac{\partial f}{\partial \alpha} \right) \\ + \frac{1}{p^2} \frac{\partial}{\partial p} \left(p^2 D_{pa} \frac{\partial f}{\partial \alpha} \right) + \frac{1}{G} \frac{\partial}{\partial \alpha} \left(G D_{ap} \frac{\partial f}{\partial p} \right) - \frac{f}{\tau} \quad (1)$$

where L is L^* (but the asterisk is dropped here and for the rest of the equations in the paper); $f(\mu, K, L, t)$ is the gyro, bounce, and drift phase-averaged PSD; p and α are the electron momentum and equatorial pitch angle; $G = T(\alpha) \sin(2\alpha)$ where $T(\alpha)$ is the approximate normalized electron bounce period in a dipole field and is equal to $1.38 - 0.32(\sin \alpha + \sqrt{\sin \alpha})$ [Schulz and Lanzerotti, 1974]; D_{LL} , D_{pp} , and D_{aa} are the bounce and drift-averaged radial, momentum, and pitch-angle diffusion coefficients, respectively, and $D_{ap} = D_{pa}$ are the mixed pitch angle-momentum diffusion coefficients; τ is the electron lifetime due to Coulomb interactions with the extended atmosphere, expressed as $E(\text{keV})^{1.5} c L^4 / 256,000 (\text{s})$, where c is the speed of light in m/s [Lyons and Thorne, 1973] (which refers the original derivation to Wentworth *et al.* [1959]; the number density in the equation has been replaced with the formula from Carpenter and Smith [1964]). To solve the model equation, the operator splitting method is used to decouple the 3D diffusion into a 1D radial diffusion part for fixed μ and K values that operates on $f(L)$ and a 2D pitch-angle/momenta diffusion part for fixed L values that operates on $f(\alpha, p)$, alternating time steps of each to calculate the 3D diffusion. The radial diffusion operator is solved using the implicit finite differencing scheme, with a time step of 3 h, L ranging from 1.0 to L_{\max} (the outer boundary, see details at the end of section 2), μ from 0.01 to $10^5 \text{ MeV}/G$, and K from 0.001 to $1000 G^{1/2} R_E$. The L grid is uniform with $\Delta L = 0.1$, while the μ and K grids are geometric with 200 μ bins and 100 K bins, respectively (uniformly distributed in logarithm space). After the radial diffusion step, at all given L shells, $f(\mu, K)$ is converted to $f(\alpha, p)$ for the pitch-angle/momenta diffusion operator, for α from 0° to 90° , $\Delta \alpha = 1^\circ$, and electron momentum from 0.3 to 10.5 MeV/c (corresponding to electron energy from 0.1 to 10 MeV) with 200 uniformly distributed momentum bins. The conversion from $f(\mu, K)$ to $f(\alpha, p)$ is performed using a dipole field for simplicity. The time step of the pitch-angle/momenta diffusion operator is 2.88 min (except for the last 2D diffusion step being 1.44 min to match the 3 h 1D radial diffusion step), and it is solved using the Crank-Nicholson method [Camporeale *et al.*, 2013]. No numerical problems with the mixed diffusion terms have been found using our numerical scheme on the dense (α, p) grid. After the 2D diffusion, $f(\alpha, p)$ is converted back to $f(\mu, K)$ at all given L for the next radial diffusion step.

[6] Specification of the diffusion coefficients is required to solve the 3D diffusion equation. The radial diffusion coefficient, $D_{LL} = D_{LL}^M + D_{LL}^E$, where D_{LL}^M is the magnetic diffusion coefficient given by $D_{LL}^M = 10^{0.506K_p - 9.325} L^{10}$, and D_{LL}^E is the electric diffusion coefficient given by $D_{LL}^E = \frac{1}{4} \left(\frac{\tilde{E}}{B_0} \right)^2 \left[\frac{T}{1 + (\omega_d T/2)^2} \right] L^6$, where $\tilde{E}(K_p) = 0.26(K_p - 1) + 0.1 \text{ mV/m}$, $B_0 = 0.311 \text{ G}$, $T = 2700 \text{ s}$, and ω_d is the electron drift frequency [Brautigam

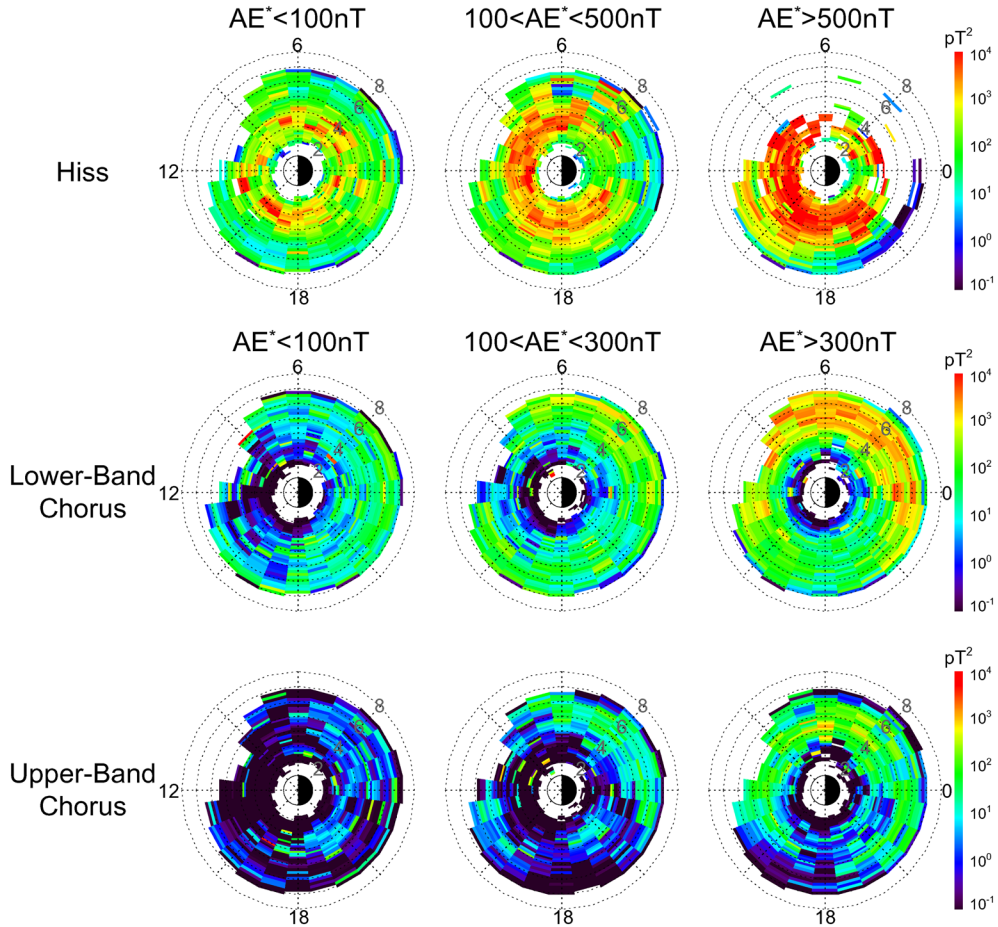
Table 1. Wave and Plasma Parameters Used for Calculating D_{aa} , D_{pp} , and D_{ap} of Lower-Band, Upper-Band Chorus, and Plasmaspheric Hiss^a

Waves	Wave Intensity Distribution	Wave Spectral Properties	Density Model
Lower-band chorus		$\omega_m/\Omega_e = 0.3, \delta\omega/\Omega_e = 0.1$ $\omega_{uc}/\Omega_e = 0.5, \omega_{lc}/\Omega_e = 0.1$	$124(3/L)^4$ [Sheeley et al. 2001]
Upper-band chorus	Dynamic wave models $B_w(\text{MLat}, \text{MLT}, L, AE^*)$	$\omega_m/\Omega_e = 0.7, \delta\omega/\Omega_e = 0.1$ $\omega_{uc}/\Omega_e = 0.9, \omega_{lc}/\Omega_e = 0.5$	$124(3/L)^4$
Plasmaspheric hiss		$\omega_m = 600\text{Hz}, \delta\omega = 300\text{Hz}$ $\omega_{uc} = 2000\text{Hz}, \omega_{lc} = 300\text{Hz}$	$10^{-0.3145L + 3.9043}$ [Carpenter and Anderson, 1992]

^aExamples of the dynamic wave model are shown in Figure 1. ω_m , $\delta\omega$, ω_{uc} , and ω_{lc} are the peak, width, upper cutoff, and lower cutoff of the truncated Gaussian distributions, respectively, assumed for the wave frequency spectra. Ω_e is the electron gyrofrequency at the magnetic equator.

and Albert, 2000]. For the pitch angle, momentum, and mixed diffusion coefficients, the method in Summers [2005] is used to calculate the bounce- and drift-averaged diffusion coefficients for field-aligned waves. Table 1 shows the wave and plasma parameters used in the calculation, which includes lower-band and upper-band chorus and plasmaspheric hiss. The wave intensity distribution for each wave type is statistically derived from the CRRES wave data, which is binned by magnetic latitude (MLat), magnetic local time (MLT), L, and AE (the mean value of AE over the previous 1 h [Li et al., 2009]). The wave intensity distributions for hiss and lower-band and upper-band chorus near the equator (MLat within 15°)

are shown in Figure 1 for three different AE* levels. These wave databases were built at LANL and validated against similar models from Meredith et al. [2003, 2004]. Based on the wave intensity distributions, the diffusion coefficients are computed corresponding to the three activity levels. Figure 2 displays the diffusion coefficients D_{aa} , D_{pp} , and D_{ap} for lower-band chorus at $L=4.5$ for the three activity levels. Similar diffusion coefficients are calculated for upper-band chorus and plasmaspheric hiss according to the parameters in Table 1. A discussion of the well-known “factor-of-two” discrepancy in the Summers [2005] diffusion coefficient calculation is included in Appendix A.

**Figure 1.** Dynamic wave models of plasmaspheric hiss, lower-band chorus, and upper-band chorus near the equator (MLat within 15°), generated from CRRES wave database. Color represents the wave intensity as a function of L and MLT for three different AE levels.

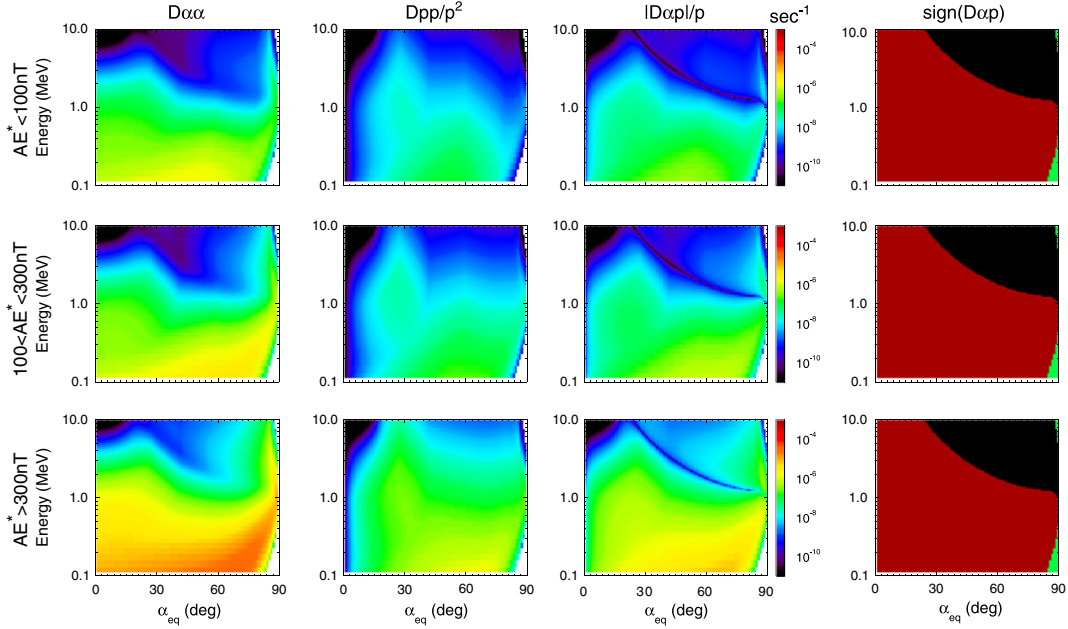


Figure 2. Calculated D_{aa} , D_{pp} , and $|D_{ap}|$ (per second) versus electron energy and equatorial pitch angle for lower-band chorus at $L=4.5$ at three different AE levels (three rows). The last column shows the sign of D_{ap} , with red being positive, black being negative, and green for zeros.

[7] The computational volume of our 3D diffusion model requires boundary conditions on six surfaces, which are specified as follows: $f(\alpha = 0^\circ) = 0$ (lost into atmosphere), $\partial f / \partial \alpha = 0$ at $\alpha = 90^\circ$, $f(L = 1) = 0$ (Earth's surface), and $f(E = 10\text{MeV}) = 0$ (very low PSD at high energy). The most important boundary conditions are the outer boundary condition at L_{\max} and the low energy boundary at $E_{\min} = 0.1\text{ MeV}$. The time-dependent CRRES PSD data are used at $L_{\max} = 5.5$ for the model μ and K grids, interpolated in time to every 3 h (radial diffusion time step). $L_{\max} = 5.5$ are chosen because the CRRES data have good coverage there. The model initial conditions are also derived from the CRRES PSD data, interpolated to the entire range of L . When CRRES was away from the geomagnetic equator, PSD at small K values (e.g., sometimes for $K < 0.01\text{ G}^{1/2}\text{R}_E$ at $L = 5.5$) are not covered by the CRRES data. To provide initial condition and outer boundary PSD at those small K values, the measured PSD are extrapolated on K in (log-PSD, linear K) space. The electron source population at E_{\min} for the 2D pitch-angle/momentum diffusion is provided by the outputs of the radial diffusion step, and is set to be constant over the 2D diffusion time steps within each 3 h interval.

[8] The general setup of our DREAM3D diffusion model is similar to that of other 3D diffusion codes which were used to simulate the CRRES intervals, e.g., the UCLA VERB model [Kim et al., 2012] and the 3D code from Albert et al. [2009]. There are, however, a few detailed differences: First, long-term simulations (for two multimonth intervals) are performed here while Kim et al. [2012] and Albert et al. [2009] simulated selected storm events with the simulation of each event initialized with the observed electron flux from CRRES. Similar long-term simulations of the CRRES data are also performed in Subbotin et al. [2011] and Kim et al. [2011, 2013]. Second, our outer boundary (O.B.) condition is taken at $L^* = 5.5$ to ensure good data coverage at the O.B. (similar to Kim et al. [2011]), while Kim et al. [2012] set the O.B. at

$L^* = 6.6$ where they assumed the electron fluxes are equal to those at $L^* = 6$ from the CRRES data, and Albert et al. [2009] set the O.B. at $L^* = 6.15$ where the flux data are processed (but note in Albert et al. [2009] L^* is calculated under the Olson-Pfizer quiet magnetic field model, which corresponds to different locations than the L^* calculated under the T89 model). Third, Albert et al. [2009] used data-driven boundary conditions at all six grid boundaries of the 3D code, while Kim et al. [2012] and the work shown here only used the data-driven boundary condition at L_{\max} . Fourth, our model has finer grid in (μ, K) and (α, p) compared to the other two models. Finally, for the calculation of the pitch angle and momentum diffusion coefficients, parallel-propagating waves are assumed here while the other two codes also include oblique waves by assuming Gaussian wave normal angle distributions.

3. Model Results

3.1. Simulation of the Training Interval: 15 August to 15 October 1990

[9] The DREAM3D diffusion model is first run for the GEM training interval (15 August to 15 October 1990), which spans two months of the CRRES mission with the most intense storm reaching minimum Dst of about -130nT . The daily-averaged CRRES PSD data (in unit of $(\text{c}/\text{MeV}/\text{cm})^3$) for $\mu = 523\text{ MeV}/\text{G}$ (corresponding to approximately 1.2 MeV electrons at $L = 4$ in a dipole) and $K = 0.03$ and $0.115\text{ G}^{1/2}\text{R}_E$ (corresponding to electron equatorial pitch angles of about 68° and 52° , respectively) are shown in the top plots of Figures 3a and 3b. In order to resolve the relative importance of radial diffusion, wave heating, and loss to the enhancement and decay of the radiation belt electrons, three different runs of the model are performed. First, the entire interval is modeled with radial diffusion (RD) only using the data-driven outer boundary condition at $L_{\max} = 5.5$ and initial condition. The

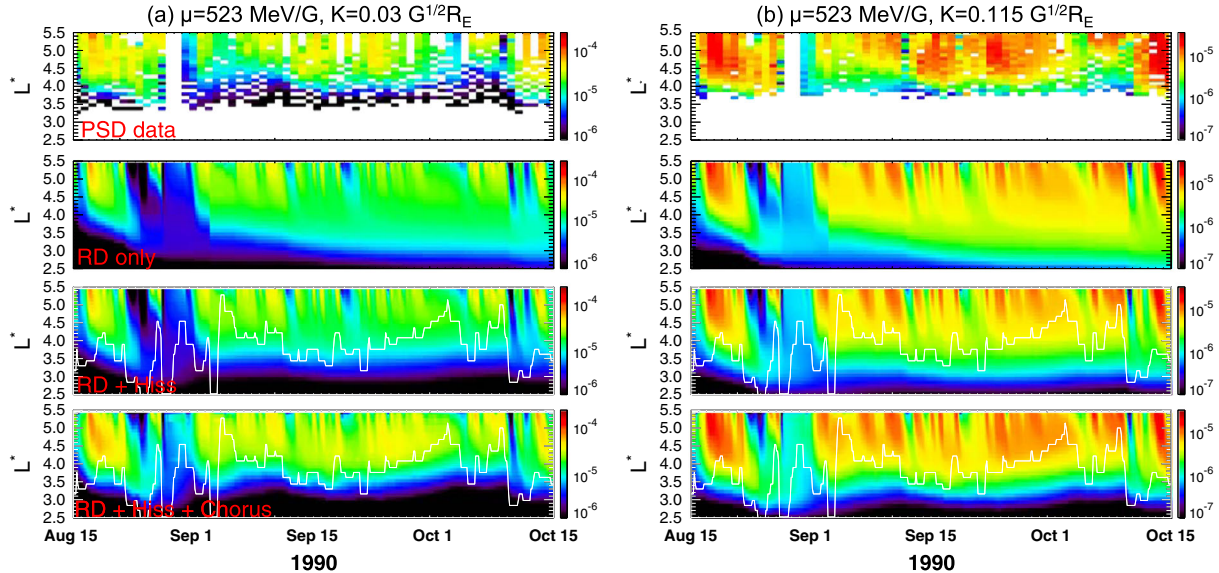


Figure 3. CRRES PSD data (in unit of $(\text{c}/\text{MeV}/\text{cm})^3$) and simulation results for the training interval (15 August to 15 October 1990), at $\mu = 523 \text{ MeV}/\text{G}$, (a) $K = 0.03 \text{ G}^{1/2} R_E$ and (b) $K = 0.115 \text{ G}^{1/2} R_E$. The top row of plots is PSD data, while the remaining rows are the model outputs with “RD only,” “RD + Hiss,” and “RD + Hiss + Chorus,” respectively. The white curves are the plasmapause locations.

results are shown in the second row of plots. Comparing the model outputs to the data, we find that radial diffusion can produce the general variations inside $L=5.5$, but it underestimates PSD at high L (e.g., some PSD data peaks around $L=4.5$) and overestimates PSD at low L (e.g., inside $L=4$). In the second run, both radial diffusion and the pitch-angle/momentum diffusion by plasmaspheric hiss inside the plasmapause are included. The plasmapause location (plotted in white) is given by the empirical model of Carpenter and Anderson [1992] as $L_{pp} = 5.6 - 0.46K_p^*$, where K_p^* is the maximum K_p value over the previous 24 h. We find (in the third row of plots) that plasmaspheric hiss produces efficient electron losses inside the plasmapause, which improves the model performance at low L . By further including the momentum and pitch angle diffusion from chorus waves outside the plasmasphere (third run with results shown in the bottom row of plots), the model can fairly well reproduce the high PSD values at large L regions (e.g., the local PSD peak on 15 September). Note that for both the second and the third runs, the mixed momentum-pitch angle diffusions are included. The simulation results also show that the fast electron dropouts across all the L regions (e.g., the dropout prior to 1 September) are well reproduced by the model. This is because the data-driven boundary condition at $L_{max} = 5.5$ already includes the reductions in PSD during those dropout events, which are then propagated to lower L regions through “outward radial diffusion,” allowing the model to capture the rapid losses over a large range of L . But this does not necessarily prove that the fast dropouts are physically due to outward radial diffusion (see discussion in section 4).

[10] To better illustrate the overestimations and underestimations from the model, the differences between the logarithm of the PSD from the model and the data shown in Figure 3a for three different runs are plotted in Figure 4a. Red means overestimation, blue indicates underestimation, and green for good reproduction. The plasmapause locations are overplotted

as black curves. It is evident in comparing “RD only” to “RD + Hiss” that adding in hiss waves reduces the overestimations inside L_{pp} , and further adding in the chorus waves (“RD + Hiss + Chorus”) greatly improves the underestimations outside L_{pp} . The electron dropouts are fairly well reproduced by all three cases (generally green during the dropouts). An interesting feature is that the code overestimates the PSD inside the plasmasphere no matter which model is used (red colors inside L_{pp} for all three runs). This may be due to the fact that the radial diffusion is too strong inside L_{pp} or that pitch angle diffusion is too slow inside L_{pp} , which will be tested in section 3.2 and further discussed in section 4.

[11] To quantitatively measure the model performance, the Mean Absolute Percentage Error (MAPE) of the model [Kim et al., 2012] is calculated:

$$\text{MAPE}(\%) = \sum_{i=1}^n \left| \frac{\log_{10}(m_i) - \log_{10}(d_i)}{\log_{10}(d_i)} \right| \times 100/n \quad (2)$$

where d_i is the PSD data, m_i is the model output, and n is the number of data points. Note that in Kim et al. [2012] d_i and m_i are electron flux but here they are PSD. Since MAPE is normalized by $|\log_{10}(d_i)|$ and the PSD values are less than 1, MAPE de-emphasizes lower PSD values (lower weights on the difference $|\log_{10}(m_i) - \log_{10}(d_i)|$ at lower PSD values in the averaging). We find that MAPE is generally $<30\%$ and on average $\sim 10\%$ when computed using all time and L for different μ and K values, proving the good performance of the model. To study the model performance for different L regions, MAPE versus L is calculated (equation (2) is summed and averaged over time) with results shown in Figure 4b for different μ and K values and from different model runs (in different colors). Even though the definition of MAPE de-emphasizes lower PSD values (generally at low L regions), we find that the model MAPE decreases as L approaches the data-derived outer boundary, where data are assimilated and it

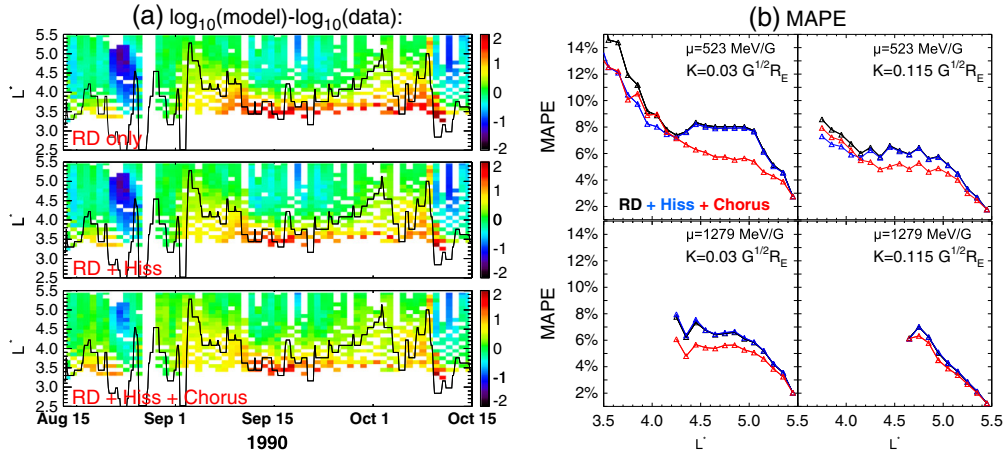


Figure 4. (a) Differences between the logarithm of the model outputs and the data shown in Figure 3a for three different runs. Red means overestimation, blue for underestimation, and green for good reproduction. The black curves on top are the plasmapause locations. (b) MAPE versus L calculated for the training interval for four pairs of (μ, K) values. Results with “RD only,” “RD + Hiss,” and “RD + Hiss + Chorus” are plotted as black, blue, and red curves, respectively.

should approach zero. On average, adding in the plasmaspheric hiss reduces the MAPE inside $L=4.2$. This is evident in the $\mu=523 \text{ MeV/G}$ results (first row), but not shown in the $\mu=1279 \text{ MeV/G}$ results since $\mu=1279 \text{ MeV/G}$ corresponds to approximately 2 MeV electrons at $L=4$ (in dipole), which is not measured by CRRES/MEA at $L < 4.2$. Including the chorus waves greatly lowers the MAPE outside $L=4.2$. In order to quantify the time dependence of the model performance, the MAPE is calculated versus time (equation (2)) is summed and averaged over L only for $2 \leq L \leq 5.5$ and the results for $\mu=523 \text{ MeV/G}$ and $K=0.03 \text{ G}^{1/2} R_E$ are shown

in Figure 5 (top panel). The variations of the geomagnetic indices (Dst , AE , and K_p) during this interval are shown at the bottom of Figure 5. Generally, the model MAPE increases during geomagnetically active times, with the run of “RD + Hiss + Chorus” generally performing the best. The improvement in MAPE from adding in chorus waves appears to be most significant during active times.

3.2. Model Sensitivity to Parameters

[12] Three types of sensitivity tests are performed on the training interval before proceeding to the challenge interval.

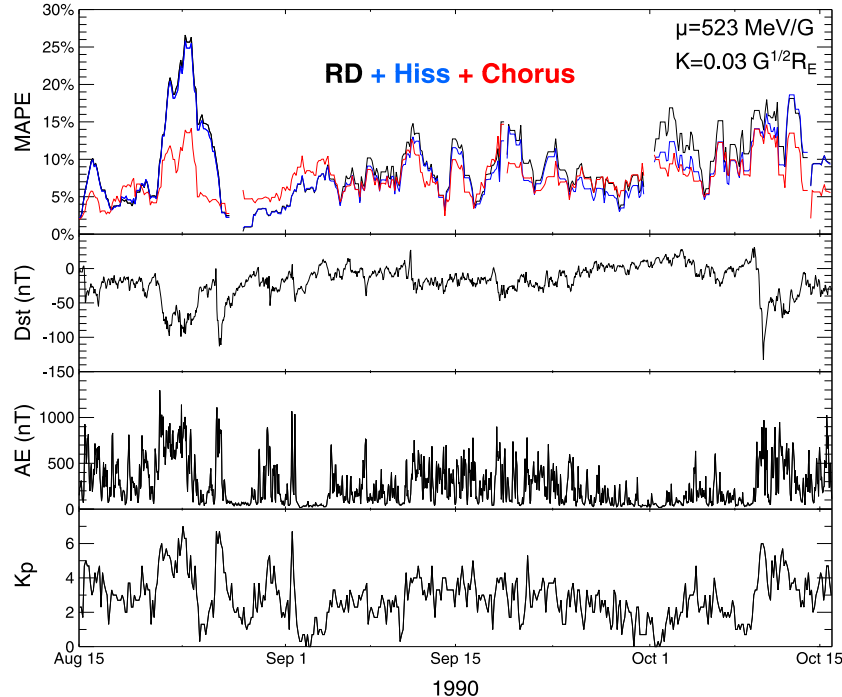


Figure 5. The top panel shows MAPE versus time calculated for the training interval for $\mu=523 \text{ MeV/G}$ and $K=0.03 \text{ G}^{1/2} R_E$. Results with “RD only,” “RD + Hiss,” and “RD + Hiss + Chorus” are plotted as black, blue, and red curves, respectively. The bottom panels show the variations of Dst , AE , and K_p indices.

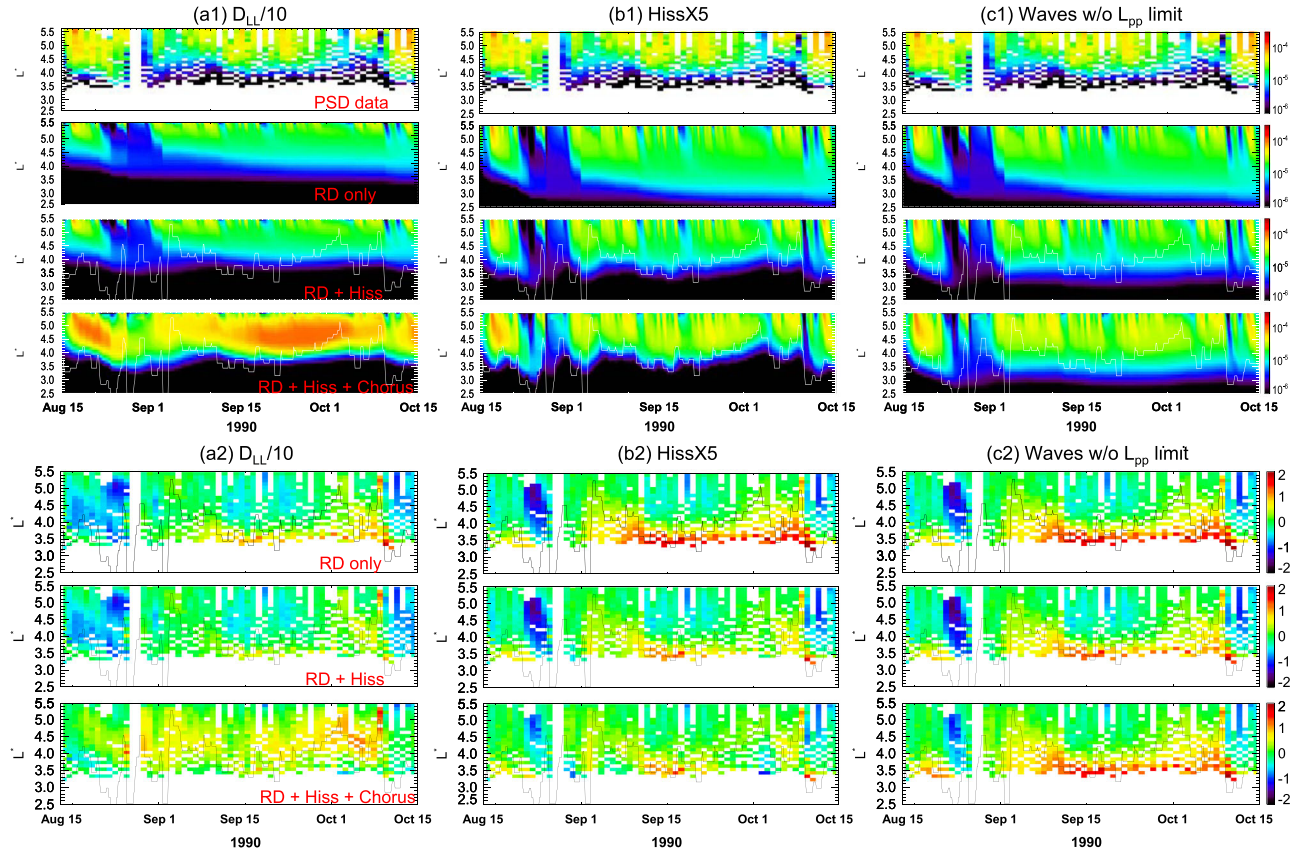


Figure 6. Top plots: CRRES PSD data ($\mu = 523$ MeV/G, $K = 0.03 G^{1/2} R_E$) and simulation results for the training interval from three different test simulations: (a) D_{LL} divided by 10, (b) hiss power multiplied by 5, and (c) not limiting chorus outside the plasmapause and hiss inside. Bottom plots: Differences between the logarithm of the model outputs and the data shown in the top plots for three different test simulations.

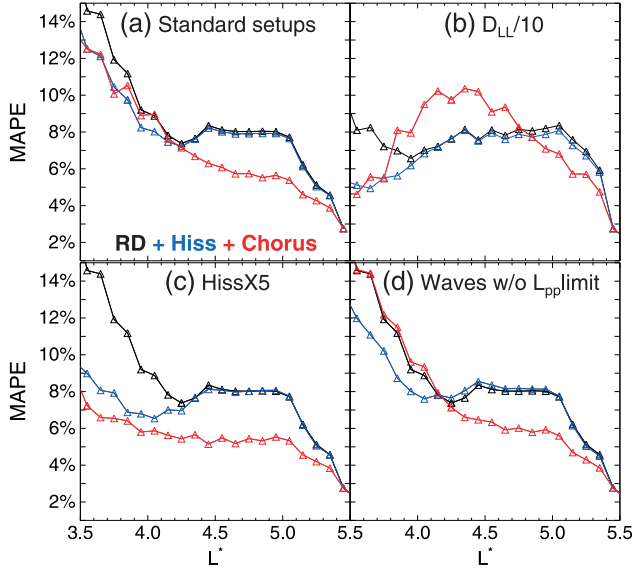


Figure 7. Comparison of MAPE versus L at $\mu = 523$ MeV/G and $K = 0.03 G^{1/2} R_E$ for the training interval from four different simulations. Figure 7a is the same with the upper left plot of Figure 4b with standard model setups. The rest of the panels are with (b) D_{LL} divided by 10, (c) hiss power multiplied by 5, and (d) not limiting chorus outside L_{pp} and hiss inside L_{pp} , respectively.

The first type involves varying the radial diffusion coefficient. The simulation results described in section 3.1 overestimate the electron PSD inside the plasmasphere (Figure 4a), which may be caused by having too strong radial diffusion inside L_{pp} . Previous studies have shown that the total radial diffusion coefficients from *Brautigam and Albert* [2000] could overestimate the physical D_{LL} by even an order of magnitude during geomagnetically active times over $L = 3-7$ [Tu et al., 2012; Ozeke et al., 2012]. Here the model sensitivity to the radial diffusion coefficient is tested by simply reducing the model D_{LL} across all the L regions by a factor of 10. The new simulation results with $D_{LL}/10$ from three different runs (“RD only,” “RD+Hiss,” and “RD+Hiss+Chorus”) are shown in Figure 6a1, with the model-data differences plotted in Figure 6a2. We find that reducing the radial diffusion rate by a factor of 10 does significantly improve the results inside the plasmasphere (comparing Figure 6a2 to Figure 4a), but in this case chorus produces too much heating outside the plasmapause (Figure 6a1). This may be due to the fact that the reduced radial diffusion is no longer strong enough to reduce the PSD by outward radial diffusion to the outer boundary. This is consistent with the sensitivity study results presented in *Albert et al.* [2009], where they showed that decreasing D_{LL} leads to larger PSD in the model, suggesting that chorus and radial diffusion compete in determining electron PSD. The results are also evident from the MAPE versus L plot for this test simulation as shown in

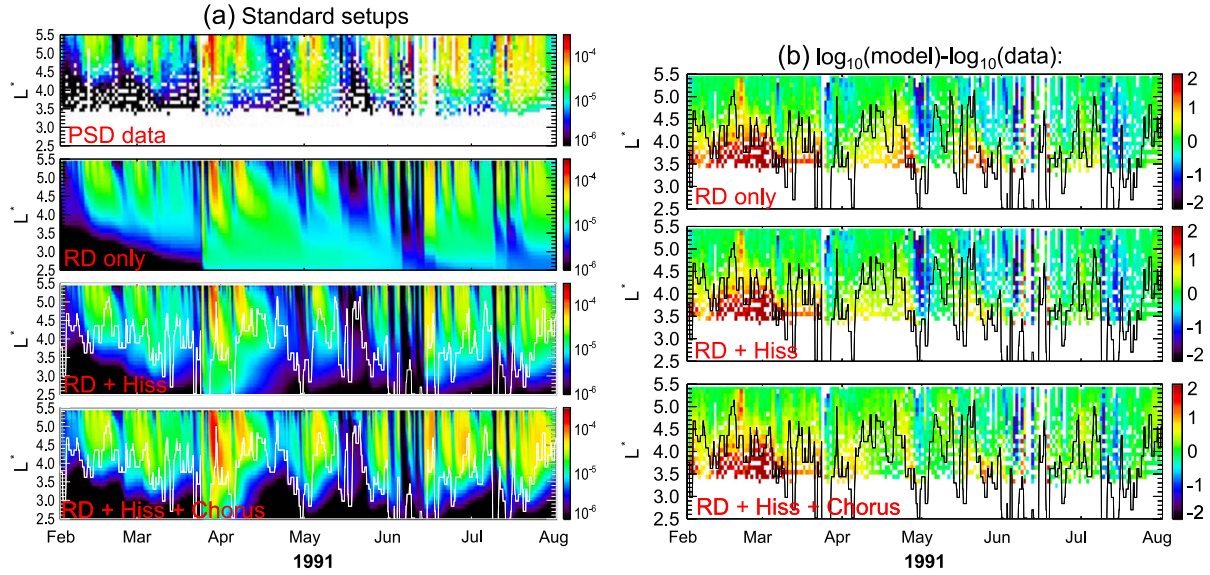


Figure 8. (a) CRRES PSD data and simulation results at $\mu = 523$ MeV/G and $K = 0.03 G^{1/2}R_E$ for the challenge interval (1 February to 31 July 1991). (b) Differences between the logarithm of the model outputs and the data.

Figure 7b. Compared with the MAPE of the standard simulation (no reduction in D_{LL}) replotted in Figure 7a, reducing D_{LL} by a factor of 10 greatly decreases the MAPE inside L_{pp} for all three runs (“RD only,” “RD+Hiss,” and “RD+Hiss+Chorus”), but “RD+Hiss+Chorus” produces much higher MAPE outside L_{pp} . Therefore, the test simulation suggests that reducing the radial diffusion coefficient over all the L regions does not improve the overall model performance.

[13] Another explanation for the model overestimation inside the plasmasphere may be due to pitch angle diffusion being too slow in that region. To test the model sensitivity to the pitch angle diffusion coefficient, the hiss wave power is increased by a factor of five so that the D_{aa} inside L_{pp} is five times larger (D_{pp} and D_{ap} from hiss will also be five times faster but they are insignificant compared to the hiss D_{aa}). The model results are shown in Figure 6b1, with the model-data differences in Figure 6b2, and the model MAPE plotted in Figure 7c. By comparing the model results and the MAPE from the standard and the new “HissX5” runs, we find that for the training interval increasing D_{aa} inside L_{pp} largely improves the model performance inside the plasmasphere. This will be further tested for the challenge interval in the next section.

[14] The final parameters tested on the training interval are the locations of the chorus and hiss waves. In the previous runs, the chorus waves are limited to be outside the plasmasphere and hiss inside (no overlap between two types of waves) due to their physical wave conditions and the fact that these limitations are commonly applied in radiation belt models [e.g., Albert *et al.*, 2009; Kim *et al.*, 2012]. The wave intensity distributions of chorus and hiss generated from CRRES data (Figure 1) actually cover all the L regions and they demonstrate consistent L and MLT dependence (hiss mostly confined to lower L regions compared to chorus waves). Therefore, instead of strictly confining chorus waves outside L_{pp} and hiss inside, the L dependence from the statistical wave models as shown in Figure 1 is directly used and the diffusion coefficients from the two types of waves are summed when they are

colocated in the wave models, which is our third test simulation. The simulation results, model-data differences, and model MAPE are plotted in Figure 6c1, Figure 6c2, and Figure 7d, respectively. The results are generally comparable to the standard runs shown in Figure 3a. However, from Figure 7d, we find that applying the chorus waves to all L regions (not limited to $>L_{pp}$), the model MAPE shows an evident increase at lower L regions, indicating higher errors compared to the previous runs (Figure 7a). Therefore, for the challenge interval chorus waves will still only be included outside the plasmasphere and hiss waves inside the plasmasphere.

3.3. Simulation of the Challenge Interval: 1 February to 31 July 1991

[15] After simulating the training interval, we now turn our attention to the GEM challenge interval (1 February to 31 July 1991) with standard model setups (D_{LL} from Brautigam and Albert [2000], hiss power from the empirical database, and chorus waves outside L_{pp} and hiss inside). The interval covers six months of the CRRES era including a lot of dynamics of the outer belt electrons. The PSD data and simulation results are shown in Figure 8a for $\mu = 523$ MeV/G and $K = 0.03 G^{1/2}R_E$ electrons, with the model-data differences plotted in Figure 8b. Again, radial diffusion can produce the general PSD variations inside $L=5.5$, including the fast PSD dropouts across all L regions. Turning on the pitch angle diffusion from plasmaspheric hiss creates efficient electron losses inside L_{pp} , and further adding in the momentum diffusion from chorus better simulates the PSD enhancements outside L_{pp} . The results show that the electron PSD inside the plasmasphere is still sometimes overestimated by the model (Figure 8b), but during many other times the model performed well across all Ls. The model MAPE for this interval are calculated and plotted in Figure 9a and Figure 10, with the corresponding geomagnetic indices shown at the bottom of Figure 10. The run with “RD+Hiss+Chorus” greatly reduces the MAPE from

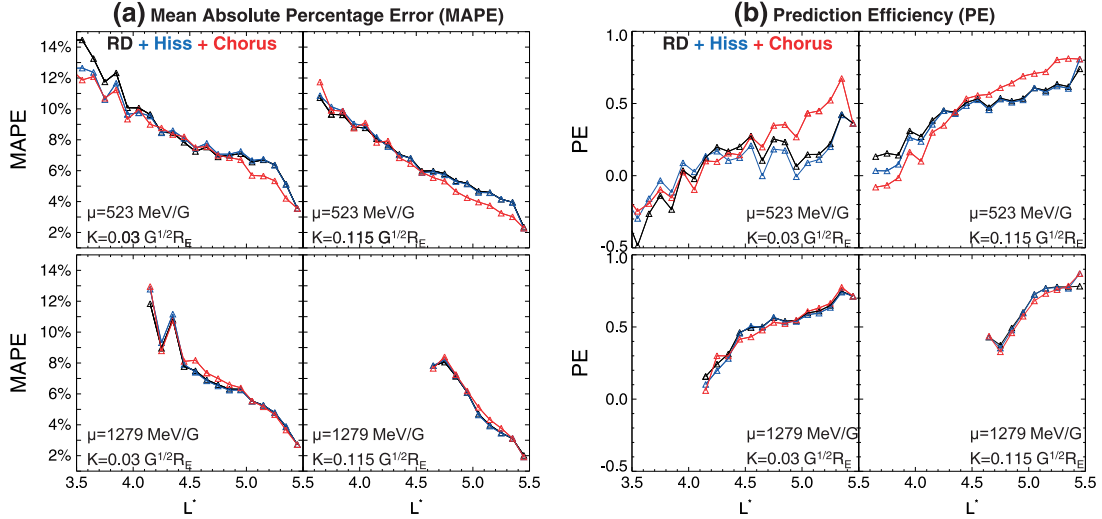


Figure 9. (a) MAPE versus L calculated for the challenge interval with the same configuration in Figure 5a. (b) PE versus L calculated for the same model results.

the ‘‘RD only’’ and ‘‘RD + Hiss’’ runs, especially during geomagnetically active times (Figure 10), and it improves the model performance at $L > L_{pp}$ (Figure 9a). For a reference, the model Prediction Efficiency (PE) versus time is also calculated and shown in Figure 9b, where $\text{PE} = 1 - \sum_i^n (\log_{10} d_i - \log_{10} m_i)^2 / \sum_i^n (\log_{10} d_i - \overline{\log_{10} d})^2$, and $\overline{\log_{10} d}$ is the mean of all $\log_{10} d_i$ [Li, 2004]. Unlike for MAPE, higher PE indicates better model performance. Note that PE does not go to 1 at the data-derived outer boundary since the outer boundary condition at $L_{\max} = 5.5$ is derived by interpolating the PSD data in L , while for

calculating PE the data d_i is computed by averaging the PSD data within each L bin (size 0.1). The PE results show similar comparison between different runs as in the MAPE results, but the improvement on PE from adding in the chorus waves appears more significant than the improvement on MAPE (e.g., the top left plots in Figures 9a and 9b).

[16] The same sensitivity test on the pitch angle diffusion coefficient introduced in section 3.2 is also performed here for the challenge interval by increasing the hiss wave power by a factor of five over the entire interval. The model results with ‘‘HissX5’’ are shown in Figure 11a with the model-data differences shown in Figure 11b. Comparing Figure 11b with

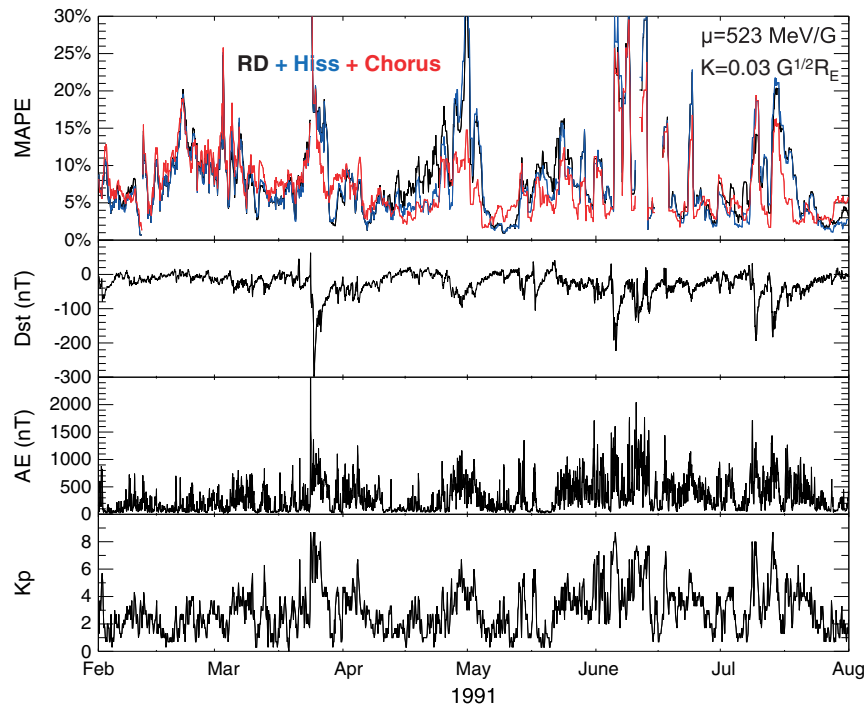


Figure 10. MAPE versus time calculated for the challenge interval with similar configuration as in Figure 6.

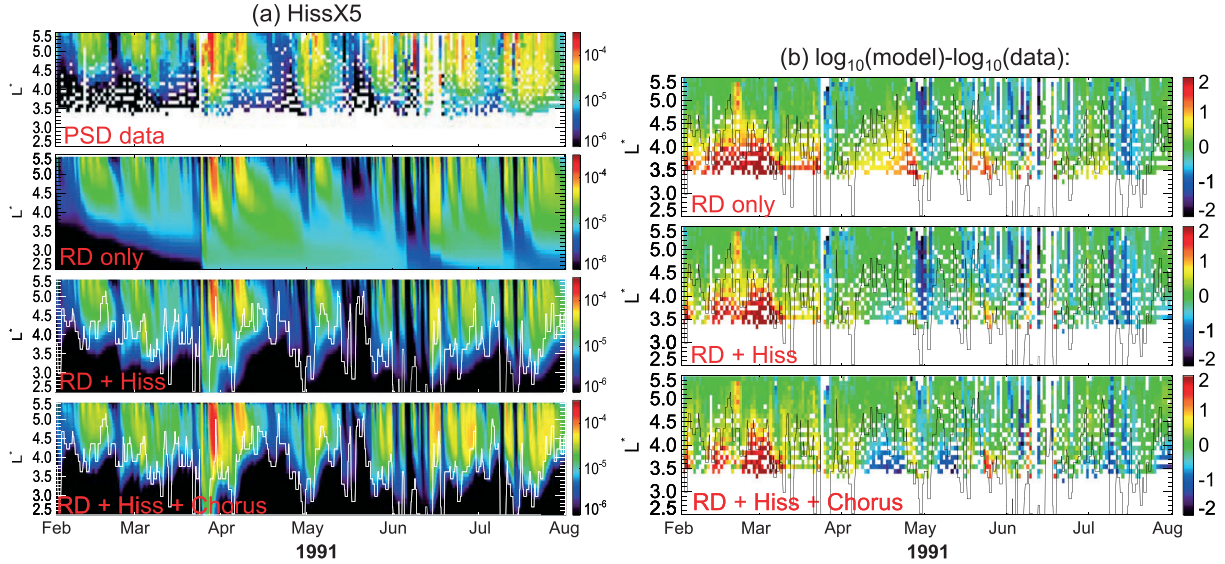


Figure 11. (a) CRRES PSD data and simulation results at $\mu = 523$ MeV/G and $K = 0.03$ G $^{1/2}$ R_E for the challenge interval with hiss power multiplied by 5. (b) Differences between the logarithm of the model outputs and the data from this test simulation.

Figure 8b from the standard runs, we find increasing D_{aa} inside L_{pp} helps improve the overestimations around March 1991, but for many other times it introduces underestimations of the PSD (e.g., between April and May 1991 inside L_{pp}). Therefore, unlike for the training interval, increasing the pitch angle diffusion coefficients inside the plasmasphere for the challenge interval does not always improve the model performance.

[17] In addition to comparing our model results with the data in PSD and (μ , K) space, it is valuable to perform the comparison in electron flux as a function of electron energy and pitch angle. The model outputs, PSD(μ , K, L), are converted to electron flux along the CRRES orbit as a function of electron energy and local pitch angle using the T89

magnetic field model to perform a direct comparison with the observed electron flux at CRRES. Figure 12a shows the daily-averaged electron flux observed by CRRES for 1.1 MeV and locally mirroring electrons (local pitch angle of 90°) during the entire challenge interval, which is compared with the model predicted flux shown in Figure 12b. The model reproduces the general variations of the electron flux, including the decreases and increases, while the overestimation inside the plasmasphere is still obvious in the flux comparison. By calculating the MAPE of flux using equation (2) (with d_i and m_i being electron flux), the variations of MAPE versus time are plotted in the bottom panel of Figure 12. This MAPE has the same definition as that used in Kim *et al.* [2012]. While MAPE for PSD de-emphasizes

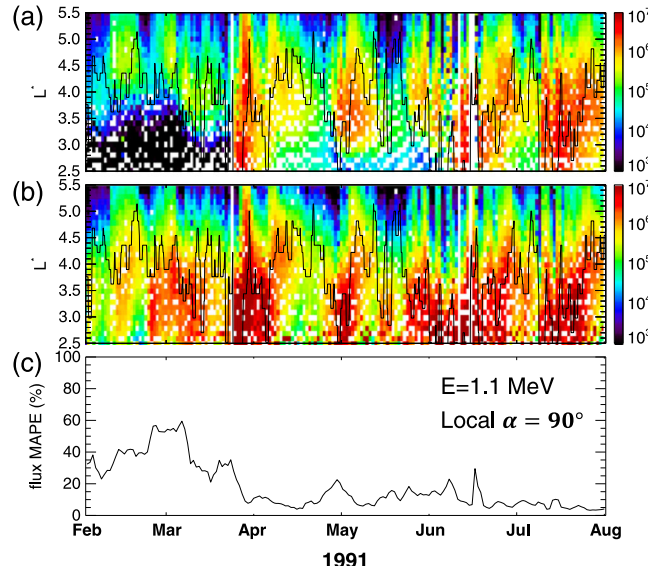


Figure 12. (a) CRRES flux data for 1.1 MeV electrons with 90° local pitch angle during the challenge interval, compared with the (b) modeled flux from the simulation with “RD + Hiss + Chorus”. The bottom panel shows the calculated MAPE of flux versus time.

Table 2. MAPE During Different Activity Levels Defined in AE, Kp, and Dst from Three Different Runs^a

MAPE%	AE (nT)			Kp			Dst (nT)		
	<100	100-300	>300	<2	2-4	>4	Quiet	Main Phase	Recov. Phase
RD only	7.33	7.62	10.40	6.89	8.11	12.08	7.87	8.46	8.63
RD + Hiss	6.43	7.05	10.27	6.00	7.52	12.30	6.90	8.21	8.71
RD + Hiss + Chorus	6.98	6.96	8.20	6.63	7.05	9.46	7.35	6.99	7.01

^aThe statistics combines results from both the training and the challenge intervals. Numbers in bold are the lowest MAPE among all three runs in each category.

the lower PSD values (see discussions below equation (2)), the MAPE for flux de-emphasizes the higher electron flux since the flux values are greater than 1. The model overestimation in the first 40 days brings the flux MAPE up to 60%, but it is generally below 20% after April. The averaged MAPE of flux over the challenge interval for 1.1 MeV and locally mirroring electrons at CRRES is ~18%, which is lower than the MAPE values published in *Kim et al.* [2012] for the same time intervals (e.g., the bottom panel of Figure 4 in *Kim et al.* [2012]). The reason for the lower MAPE from our model may be that the PSD reductions are included in our outer boundary condition at $L_{\max} = 5.5$ (see detailed discussion in section 4).

3.4. Overall Statistics

[18] It is useful to calculate the MAPE during different activity levels to statistically investigate the dependence of the model performance on geomagnetic activity. Here, the training and challenge intervals (8 months in total) are combined to classify the time into different activity levels by AE, Kp, and Dst, respectively. Table 2 includes the MAPE (calculated from equation (2) summed and averaged over time and L) from the model during three different AE, Kp, and Dst levels. The results show that, statistically, the run with “RD + Hiss” performs the best during relatively quiet times ($AE < 100$ nT, $Kp < 2$, and Dst quiet times, with the lowest MAPE among three runs marked in red), while adding in both hiss and chorus (the third run) best reproduces the data variations during geomagnetically active times.

4. Discussion

[19] Our DREAM3D diffusion model, driven by data-derived outer boundary condition at $L_{\max} = 5.5$ and initial condition, includes the effects of radial diffusion (empirically parameterized by Kp index) and pitch angle and momentum diffusion from dynamic wave models of lower-band chorus, upper-band chorus, and plasmaspheric hiss. Perhaps because our outer boundary is set up at $L_{\max} = 5.5$, the model results have smaller errors compared to those from other 3D diffusion models, e.g., *Kim et al.* [2012], for the same GEM challenge interval and *Albert et al.* [2009] for the October 1990 storm. With a data-driven outer boundary condition at $L_{\max} = 5.5$, our model results better capture the fast electron dropouts observed in the data. At $L_{\max} = 5.5$, the PSD reductions are already included at the outer boundary, which are then propagated to the lower L regions allowing our model to accommodate the fast electron dropouts across a large range of L without having an explicit model of the loss process. Other work, e.g., *Kim et al.* [2012], tried to capture more of the radiation belt in L by setting the outer boundary at

$L_{\max} = 6.6$ and extrapolating the flux data from $L = 6$ to 6.6 as the boundary condition. The electron dropouts are less well reproduced in this work with a boundary condition at larger L due to the lack of an explicit model for various loss processes. Using a directly data-driven boundary condition at $L_c = 5.5$, though sacrificing the L coverage, produces a better prediction of the interior PSD changes. However, in order to physically resolve the underlying mechanisms for the fast electron dropouts, a model with a realistic outer boundary condition at the magnetopause is needed to simulate losses from the magnetopause shadowing and outward radial diffusion, and the inclusion of other wave populations that can produce pitch angle diffusion is also required (e.g., EMIC waves). These processes will be included in future versions of the DREAM3D model.

[20] The model sensitivity to the diffusion coefficients has been tested in section 3.2, which quantitatively demonstrated the competition between radial diffusion, wave heating, and pitch-angle scattering in determining the radiation belt dynamics. Specifically, from Figures 4 and 8, we find that even with all the effects of radial diffusion, chorus, and plasmaspheric hiss included, the model still often overestimates the PSD inside the plasmapause. This may either be due to radial diffusion that is too strong or pitch angle diffusion that is too slow in that region. The first hypothesis is tested by reducing the radial diffusion coefficients across all Ls by a factor of 10 for the training interval. The results in section 3.2 suggest that it improves the model performance inside L_{pp} but leads to overestimation outside L_{pp} . The second hypothesis is tested by increasing the pitch angle diffusion coefficients inside L_{pp} by a factor of five for both the training and the challenge intervals. The results show that it sometimes works to reduce the overestimations inside L_{pp} but for many other times it actually introduces underestimations in the model. Thus, neither of these two explanations, radial diffusion that is too strong or pitch angle diffusion that is too slow, can be applied to solve all the mismatches from the model. In order to fully explain the observed electron dynamics at different L regions and times, better wave models than the current ones binned by AE index, and a better radial diffusion model than the Kp-dependent D_{LL} from *Brautigam and Albert* [2000], are required. For example, the results already demonstrate that reducing the D_{LL} over all the L regions improves the model performance inside L_{pp} but worsens the performance outside L_{pp} , which leads us to wonder what would happen if we only reduce the D_{LL} inside L_{pp} . Studies have shown that the total radial diffusion coefficients from *Brautigam and Albert* [2000] could overestimate the physical D_{LL} by an order of magnitude over a wide L range ($L = 3\text{--}7$) [*Tu et al.*, 2012; *Ozeke et al.*, 2012], but none of these

studies were focused on the detailed D_{LL} inside the plasmasphere, where the ULF wave properties can be very different from those outside the plasmasphere. The D_{LL} technique developed by the University of Alberta group based on the ground magnetometer data [Ozeke *et al.*, 2012] can be very useful to this study. When the more realistic D_{LL} model becomes available in the future, the empirical Kp-driven radial diffusion coefficients used in the model will be replaced with more physical ones derived from the ground and space field measurements to test the effects on our model performance.

[21] The overall statistics from our model in section 3.4 suggest that radial diffusion combined with the pitch angle diffusion from plasmaspheric hiss is adequate to explain the outer belt dynamics during quiet times. This is consistent with the results published in Lyons and Thorne [1973], which reproduced the quiet time two-belt structure of the Earth's radiation belts based on the balance between radial diffusion and pitch angle scattering by hiss. During geomagnetically quiet times, radial diffusion propagates the variability present from the data at the outer boundary to inner L regions, which, combined with the pitch angle diffusion by hiss inside the plasmasphere, generally accounts for the observed electron dynamics inside $L_{max} = 5.5$. During active times, wave activities reach deeper into the magnetosphere and the local heating from chorus becomes more important.

[22] The mixed pitch angle-momentum diffusion terms in equation (1) have been shown to play the role of limiting local heating from chorus waves, especially for higher-energy electrons (>1 MeV) with lower equatorial pitch angles ($<30^\circ$) [Albert *et al.*, 2009; Kim *et al.*, 2012]. The presence of radial diffusion is also found to reduce the effects of the mixed diffusion terms [Albert *et al.*, 2009]. Our model demonstrates similar effects of the mixed diffusion terms that are consistent with the previous studies (not shown).

[23] Finally, we discuss the possible sources of error due to the model assumptions. First, the calculation of momentum, pitch angle, and mixed diffusion coefficients currently assumes parallel-propagating waves following the Summers [2005] approach. There is increasing observational and theoretical evidence of oblique chorus and hiss waves in the radiation belts [Li *et al.*, 2011; Bortnik *et al.*, 2011], which could significantly affect the pitch angle and momentum diffusion coefficients derived from the wave properties [Albert, 2008]. For example, including oblique hiss at high latitude in the diffusion coefficient calculation may increase its pitch angle diffusion rate, improving the overestimation problem of our model inside the plasmasphere. Therefore, as a future improvement full wave normal angle distributions will be included in the diffusion coefficient calculations and test their effects on the model results. Second, a dipole field is assumed for the computation of momentum, pitch angle, and mixed diffusion coefficients, while Orlova *et al.* [2012] showed that using a realistic magnetic field model can make a significant difference in the calculated scattering rate for >1 MeV electrons during geomagnetically active times. Third, in our model equation (equation (1)), the pitch-angle-momentum diffusion is assumed to not cause radial diffusion and vice versa, thus the mixed radial-pitch angle diffusion and radial-momentum diffusion terms are not included. Radial diffusion cannot cause pitch-angle/momentun diffusion since the interactions with ULF waves, which generate

radial diffusion, can only violate the third adiabatic invariant but not fast enough to violate the first and second adiabatic invariants. On the other hand, pitch-angle/momentun diffusion generated by wave-particle interactions with higher frequency waves (faster than MeV electrons' drift frequency) can also break the third adiabatic invariant and cause radial diffusion, leading to nonzero mixed diffusion terms. The significance of the mixed radial-pitch angle and radial-momentum diffusion is still an outstanding question which deserves quantitative studies.

5. Conclusions

[24] In this paper the radiation belt electron dynamics during two intervals of the CRRES mission are simulated using our DREAM3D diffusion model. The two intervals, 15 August to 15 October 1990 and 1 February to 31 July 1991, are defined as the training and challenge intervals by the GEM/RBWM focus group for the "Global Radiation Belt Modeling Challenge." Our 3D diffusion model, DREAM3D, includes radial, pitch angle, and momentum diffusion and mixed pitch angle-momentum diffusion of radiation belt electrons. The momentum, pitch angle, and mixed diffusion coefficients are derived from dynamic wave models of upper-band and lower-band chorus and plasmaspheric hiss, which are statistically generated from the CRRES wave data. The outer boundary condition at $L_{max} = 5.5$ and the initial condition of the model are both extracted from the CRRES PSD data.

[25] By comparing the model results to the PSD data and quantifying the model performance using Mean Absolute Percentage Error (MAPE) and Prediction Efficiency (PE), we find that with a data-driven outer boundary condition at $L_{max} = 5.5$, radial diffusion can generally explain the variations of radiation belt electrons, including the fast electron dropouts across wide L regions. Additional local heating from chorus waves is required to reproduce the fast and strong PSD enhancements outside the plasmapause and plasmaspheric hiss is efficient in producing electron losses inside the plasmasphere. The model can capture the fast electron dropouts well because the PSD reductions are already included in the $L_{max} = 5.5$ boundary condition, which are then propagated inward by outward radial diffusion, allowing the code to accommodate rapid losses over a large L range without having an explicit model of the loss processes. This enables better performance of our model compared to previous published results. The model is found to sometimes overestimate the PSD inside the plasmasphere no matter what model is used ("RD only," "RD+Hiss," and "RD+Hiss+Chorus"), which may be due to the fact that radial diffusion is too strong inside the plasmasphere or pitch angle diffusion is too slow. This is tested by reducing the radial diffusion coefficients and increasing the pitch angle diffusion coefficients inside the plasmasphere in the model. The test simulation results suggest that in order to fully explain the observed electron dynamics at various L regions and times, we need to implement better wave models than the current ones binned by AE index and a more realistic radial diffusion model than the Kp-dependent D_{LL} from Brautigam and Albert [2000], for regions both inside and outside the plasmasphere. Finally, by statistically investigating the model performance at different geomagnetic activity levels, we conclude that

including radial diffusion and plasmaspheric hiss in the model is sufficient to simulate the radiation belt electron variations during geomagnetically quiet times, while for active times ($\text{AE} > 100 \text{ nT}$, $K_p > 2$, and storm main phases and recovery phases), the pitch angle and momentum diffusion from chorus waves are required to best capture the electron variations.

Appendix A: Discussion on “Factors-of-Two” for D_{aa} , D_{pp} , and D_{ap}

[26] In this appendix, we detail the assumptions used in our implementation of *Summers* [2005] for computing bounce-averaged diffusion coefficients, including a “factor-of-two correction” that has been mentioned in other work but for which we have a new (and hopefully clearer) explanation.

[27] A Gaussian distribution of wave power as a function of frequency is assumed, as in *Summers* [2005]. We also assume that the wave power is evenly partitioned between forward- and backward-propagating directions, consistent with the assumption in *Lyons* [1974b; Appendix A] that the distribution in positive and negative wave normal angles is symmetric. Because we assume that there is equal wave power in both forward and backward-propagating directions, we include resonant roots that have both positive and negative signs for values of $y = ck/\omega$, but assign exactly half of the observed wave power to each root when computing the sum in *Summers* [2005] equations (17)–(19). The distribution of power as a function of wave number that is assumed in *Summers* [2005] appears to be one sided, since the text following equation (30) suggests that only wave numbers of one sign are used when equating the distribution of wave power in frequency to a distribution of power in wave number. This discrepancy means that our local diffusion coefficients are a “factor of two” smaller than what would be obtained by applying the total observed wave power (summed over both propagation directions) in the *Summers* [2005] approach to all of the resonant roots. Of course, if one uses a model that has only backward-propagating waves, then the observed wave power will be concentrated only in one propagation direction, as in *Summers* [2005], but then only resonant roots that satisfy $y = ck/\omega < 0$ should be used in the sum. We show at the end of this Appendix that a different factor of two arises in this situation when you do the bounce average. Figure 3 of *Summers* [2005] shows diffusion coefficients that are calculated assuming that the propagation direction is backward-only versus both forward and backward. It is apparent that the same distribution of wave intensity as a function of frequency is used for both forward and backward-propagating directions, and so the total wave intensity integrated over both frequency and wave number is not constant for the two models presented in this figure — the total integrated wave power for the forward + backward propagation is twice that of the backward-only propagation model.

[28] Our explanation of the “factor-of-two” problem is different than what has been described earlier [*Albert*, 2007; *Tao et al.*, 2012]. *Albert* [2007] also finds a factor-of-two discrepancy between the diffusion coefficients calculated by *Summers* [2005] and his independent implementation of a parallel-propagating model, but he “tentatively ascribes” the difference to “the explicit factor of two in equation (1) of *Summers* [2005], which is not apparent in earlier work.”

We agree with *Liu et al.* [2011], though, who explain that the factor of two pointed to by *Albert* [2007] is due to a difference in how the R-mode and L-mode electric field vectors are defined. In *Lerche* [1968], which is the basis for *Summers* [2005], the R-mode and L-mode electric field vectors are defined as $E_{R,L} = E_x \mp iE_y$, whereas *Kennel and Engelmann* [1966] and *Lyons* [1974a, 1974b] define the R- and L-mode electric field vectors as $E_{R,L} = \frac{E_x \mp iE_y}{\sqrt{2}}$. Substituting in the *Lyons* [1974a, 1974b] definition of the R-mode and L-mode electric field vectors into the *Summers* [2005] equation (1) eliminates the factor of two pointed to by *Albert* [2007]. We believe that our explanation also resolves the discrepancy between the test-particle simulations of *Tao et al.* [2011] and the diffusion coefficients calculated using *Summers* [2005]. In *Tao et al.* [2011], a random wavefield is constructed as the sum of weighted cosines and sines. However, if one rewrites the expansion as a weighted sum of complex exponentials containing both positive and negative frequencies, one can show that this random wavefield is consistent with partitioning the wave power equally into positive and negative wave numbers. Thus, a calculation using *Summers* [2005] incorporating a sum over all resonant roots with the total wave power used to weight each root will produce diffusion coefficients that are a factor of two too high, as is observed by *Tao et al.* [2011]. The explanation for this discrepancy is given in the first paragraph of this Appendix.

[29] The bounce-averaging approach outlined in *Lyons et al.* [1972] is implemented using values for the local diffusion coefficient as discussed above (i.e., include all resonant roots and assume that half of the total wave power exists in each propagation direction so that the *Summers* [2005] diffusion coefficients are divided by two when the total wave power is used to normalize the sum over resonant roots). Due to the symmetry of the resonance condition as it relates to the sign of the particle’s parallel velocity and the sign of the wave normal angle, the symmetry of the dispersion relation, and the fact that a centered dipole field and plasma density model that are North-South symmetric are used, we only need to compute the bounce-averaged integral over one quarter of a bounce period since the other three quarter-bounces will produce the same roots (and weights) as a function of latitude. We note, however, that if the wave power is not equally distributed in the parallel and antiparallel directions, the correct bounce-averaged result can still be computed using the average wave power in the parallel and antiparallel directions in place of the total wave power. Since the average wave power is a factor of two less than the total wave power, the “factor of two” again makes an appearance even though in this case the local diffusion coefficients calculated using *Summers* [2005] may be correct because there may be power in only one propagation direction. In this case, the reason that a factor of two reduces the diffusion coefficient is because the resonant roots that are used for a given wave propagation direction are only used for every other quarter-bounce period (and the other resonant roots are used for the interleaving quarter-bounces). The fact that the average wave power spectral density should be used instead of the integrated total wave power is in contrast to *Orlova and Shprits* [2011], who state that the wave power spectral density should be “replaced by their sum,” whereas we contend that the average wave power spectral density should be used.

[30] We conclude that, if the desire is to produce a bounce-averaged diffusion coefficient using the Summers [2005] approach with magnetic field and plasma density models that are North-South symmetric, then independent of the intensity of the waves in each propagation direction, it is correct to (a) use the total wave power integrated over both propagation directions divided by a factor of two, and (b) use all the resonant roots.

[31] **Acknowledgments.** We gratefully acknowledge the support of the US Department of Energy through the LANL Laboratory Directed Research and Development (LDRD) Program for this work.

[32] Robert Lysak thanks Mary Hudson and an anonymous reviewer for their assistance in evaluating this paper.

References

- Abel, B., and R. M. Thorne (1998), Electron scattering loss in Earth's inner magnetosphere 1. Dominant physical processes, *J. Geophys. Res.*, **103**(A2), 2385–2396.
- Albert, J. M. (2003), Evaluation of quasi-linear diffusion coefficients for EMIC waves in a multispecies plasma, *J. Geophys. Res.*, **108**(A6), 1249, doi:10.1029/2002JA009792.
- Albert, J. M. (2007), Simple approximations of quasi-linear diffusion coefficients, *J. Geophys. Res.*, **112**, A12202, doi:10.1029/2007JA012551.
- Albert, J. M. (2008), Efficient approximations of quasi-linear diffusion coefficients in the radiation belts, *J. Geophys. Res.*, **113**, A06208, doi:10.1029/2007JA012936.
- Albert, J. M. (2012), Dependence of quasi-linear diffusion coefficients on wave parameters, *J. Geophys. Res.*, **117**, A09224, doi:10.1029/2012JA017718.
- Albert, J. M., N. P. Meredith, and R. B. Horne (2009), Three-dimensional diffusion simulation of outer radiation belt electrons during the 9 October 1990 magnetic storm, *J. Geophys. Res.*, **114**, A09214, doi:10.1029/2009JA014336.
- Baker, D. N. (2001), Satellite anomalies due to space storms, in *Space Storms and Space Weather Hazards*, NATO Sci. Ser. 2, vol. 38, edited by I. A. Daglis, pp. 285–311, Kluwer Acad, Dordrecht, Netherlands.
- Baker, D. N., and S. Kanekal (2008), Solar cycle changes, geomagnetic variations, and energetic particle properties in the inner magnetosphere, *J. Atmos. Sol. Terr. Phys.*, **70**(2-4), 195–206, doi:10.1016/j.jastp.2007.08.031.
- Bortnik, J., L. Chen, W. Li, R. M. Thorne, N. P. Meredith, and R. B. Horne (2011), Modeling the wave power distribution and characteristics of plasmaspheric hiss, *J. Geophys. Res.*, **116**, A12209, doi:10.1029/2011JA016862.
- Bourdarie, S., D. Boscher, T. Beutier, J. A. Sauvaud, and M. Blanc (1997), Electron and proton radiation belt dynamic simulations during storm periods: A new asymmetric convection-diffusion model, *J. Geophys. Res.*, **102**(A8), 17,541–17,552.
- Brautigam, D. H., and J. M. Albert (2000), Radial diffusion analysis of outer radiation belt electrons during the 9 October 1990 magnetic storm, *J. Geophys. Res.*, **105**, 291–309, doi:10.1029/1999JA900344.
- Camporeale, E., G. L. Delzanno, S. Zaharia, and J. Koller (2013), On the numerical simulation of particle dynamics in the radiation belt. Part I: implicit and semi-implicit schemes, *J. Geophys. Res. Space Physics*, **118**, 3463–3475, doi:10.1002/jgra.50293.
- Carpenter, D. L., and R. R. Anderson (1992), An ISEE/whistler model of equatorial electron density in the magnetosphere, *J. Geophys. Res.*, **97**, 1097–1108, doi:10.1029/91JA01548.
- Carpenter, D. L., and R. L. Smith (1964), Whistler measurements of electron density in the magnetosphere, *Rev. Geophys.*, **2**, 415–441.
- Chu, F., M. K. Hudson, P. Haines, and Y. Shprits (2010), Dynamic modeling of radiation belt electrons by radial diffusion simulation for a 2 month interval following the 24 March 1991 storm injection, *J. Geophys. Res.*, **115**, A03210, doi:10.1029/2009JA014409.
- Elkington, S. R., M. K. Hudson, and A. A. Chan (2003), Resonant acceleration and diffusion of outer zone electrons in an asymmetric geomagnetic field, *J. Geophys. Res.*, **108**(A3), 1116, doi:10.1029/2001JA009202.
- Fennell, J. F., H. C. Koons, J. L. Roeder, and J. B. Blake (2001), Spacecraft charging: Observations and relationship to satellite anomalies, in Proceedings of 7th Spacecraft Charging Technology Conference, Eur. Space Agency Spec. Publ., ESA SP-476, p. 279.
- Fok, M.-C., R. B. Horne, N. P. Meredith, and S. A. Glauert (2008), Radiation Belt Environment model: Application to space weather nowcasting, *J. Geophys. Res.*, **113**, A03S08, doi:10.1029/2007JA012558.
- Fraser, B. J., and T. S. Nguyen (2001), Is the plasmapause a preferred source region of electromagnetic ion cyclotron waves in the magnetosphere?, *J. Atmos. Sol. Terr. Phys.*, **63**(1225), 2001.
- Fu, H. S., J. B. Cao, B. Yang, and H. Y. Lu (2011), Electron loss and acceleration during storm time: The contribution of wave-particle interaction, radial diffusion, and transport processes, *J. Geophys. Res.*, **116**, A10210, doi:10.1029/2011JA016672.
- Horne, R. B., and R. M. Thorne (1998), Potential waves for relativistic electron scattering and stochastic acceleration during magnetic storms, *Geophys. Res. Lett.*, **25**(15), 3011–3014, doi:10.1029/98GL01002.
- Horne, R. B., R. M. Thorne, S. A. Glauert, J. M. Albert, N. P. Meredith, and R. R. Anderson (2005), Timescale for radiation belt electron acceleration by whistler mode chorus waves, *J. Geophys. Res.*, **110**, A03225, doi:10.1029/2004JA010811.
- Horne, R. B., R. M. Thorne, S. A. Glauert, N. P. Meredith, D. Pokhotelov, and O. Santolík (2007), Electron acceleration in the Van Allen radiation belts by fast magnetosonic waves, *Geophys. Res. Lett.*, **34**, L17107, doi:10.1029/2007GL030267.
- Hudson, M. K., S. R. Elkington, J. G. Lyons, and C. C. Goodrich (2000), Increase in relativistic electron flux in the inner magnetosphere: ULF wave mode structure, *Adv. Space Res.*, **25**, 2327–2337.
- Kennel, C. F., and F. Engelmann (1966), Velocity space diffusion from weak plasma turbulence in a magnetic field, *Phys. Fluids*, **9**, 2377–2388.
- Kessel, R. L., N. J. Fox, and M. Weiss (2012), The Radiation Belt Storm Probes (RBSP) and Space Weather, *Space Sci. Rev.*, doi:10.1007/s11214-012-9953-6.
- Kim, K.-C., and Y. Shprits (2013), Long-term relativistic radiation belt electron responses to GEM magnetic storms, *J. Atmos. Sol. Terr. Phys.*, **100–101**, 59–67, doi:10.1016/j.jastp.2013.04.007.
- Kim, K.-C., Y. Shprits, D. Subbotin, and B. Ni (2011), Understanding the dynamic evolution of the relativistic electron slot region including radial and pitch angle diffusion, *J. Geophys. Res.*, **116**, A10214, doi:10.1029/2011JA016684.
- Kim, K.-C., Y. Shprits, D. Subbotin, and B. Ni (2012), Relativistic radiation belt electron responses to GEM magnetic storms: Comparison of CRRES observations with 3-D VERB simulations, *J. Geophys. Res.*, **117**, A08221, doi:10.1029/2011JA017460.
- Lerche, I. (1968), Quasilinear theory of resonant diffusion in a magnetically active relativistic plasma, *Phys. Fluids*, **11**, 1720.
- Li, X. (2004), Variations of 0.7–6.0 MeV electrons at geosynchronous orbit as a function of solar wind, *Space Weather*, **2**, S03006, doi:10.1029/2003SW000017.
- Li, X., D. Baker, M. Temerin, T. Cayton, E. Reeves, R. Christensen, J. Blake, M. Looper, R. Nakamura, and S. Kanekal (1997), Multisatellite observations of the outer zone electron variation during the November 3–4, 1993, magnetic storm, *J. Geophys. Res.*, **102**(A7), 14,123–14,140.
- Li, W., Y. Y. Shprits, and R. M. Thorne (2007), Dynamic evolution of energetic outer zone electrons due to wave-particle interactions during storms, *J. Geophys. Res.*, **112**, A10220, doi:10.1029/2007JA012368.
- Li, W., R. M. Thorne, V. Angelopoulos, J. Bortnik, C. M. Cully, B. Ni, O. LeContel, A. Roux, U. Auster, and W. Magnes (2009), Global distribution of whistler-mode chorus waves observed on the THEMIS spacecraft, *Geophys. Res. Lett.*, **36**, L09104, doi:10.1029/2009GL037595.
- Li, W., J. Bortnik, R. M. Thorne, and V. Angelopoulos (2011), Global distribution of wave amplitudes and wave normal angles of chorus waves using THEMIS wave observations, *J. Geophys. Res.*, **116**, A12205, doi:10.1029/2011JA017035.
- Liu, K., D. S. Lemons, D. Winske, and S. P. Gary (2010), Relativistic electron scattering by electromagnetic ion cyclotron fluctuations: Test particle simulations, *J. Geophys. Res.*, **115**, A04204, doi:10.1029/2009JA014807.
- Liu, K., S. P. Gary, and D. Winske (2011), Excitation of magnetosonic waves in the terrestrial magnetosphere: Particle-in-cell simulations, *J. Geophys. Res.*, **116**, A07212, doi:10.1029/2010JA016372.
- Loto'aniu, T. M., R. M. Thorne, B. J. Fraser, and D. Summers (2006), Estimating relativistic electron pitch angle scattering rates using properties of the electromagnetic ion cyclotron wave spectrum, *J. Geophys. Res.*, **111**, A04220, doi:10.1029/2005JA011452.
- Lyons, L. R. (1974a), General relations for resonant particle diffusion in pitch angle and energy, *J. Plasma Phys.*, **12**, 45–49.
- Lyons, L. R. (1974b), Pitch angle and energy diffusion coefficients from resonant interactions with ion-cyclotron and whistler waves, *J. Plasma Phys.*, **12**, 417–432.
- Lyons, L. R., and R. M. Thorne (1973), Equilibrium structure of radiation belt electrons, *J. Geophys. Res.*, **78**(13), 2142–2149, doi:10.1029/JA078i013p02142.
- Lyons, L. R., R. M. Thorne, and C. F. Kennel (1972), Pitch-angle diffusion of radiation belt electrons within the plasmasphere, *J. Geophys. Res.*, **77**(19), 3455–3474, doi:10.1029/JA077i019p03455.

- Meredith, N. P., R. B. Horne, R. H. A. Iles, R. M. Thorne, D. Heynderikx, and R. R. Anderson (2002), Outer zone relativistic electron acceleration associated with substorm-enhanced whistler mode chorus, *J. Geophys. Res.*, **107**(A7), 1144, doi:10.1029/2001JA900146.
- Meredith, N. P., R. B. Horne, R. M. Thorne, and R. R. Anderson (2003), Favored regions for chorus-driven electron acceleration to relativistic energies in the Earth's outer radiation belt, *Geophys. Res. Lett.*, **30**(16), 1871, doi:10.1029/2003GL017698.
- Meredith, N. P., R. B. Horne, R. M. Thorne, D. Summers, and R. R. Anderson (2004), Substorm dependence of plasmaspheric hiss, *J. Geophys. Res.*, **109**, A06209, doi:10.1029/2004JA010387.
- Meredith, N. P., R. B. Horne, S. A. Glauert, and R. R. Anderson (2007), Slot region electron loss timescales due to plasmaspheric hiss and lightning-generated whistlers, *J. Geophys. Res.*, **112**, A08214, doi:10.1029/2007JA012413.
- Miyoshi, Y. S., V. K. Jordanova, A. Morioka, M. F. Thomsen, G. D. Reeves, D. S. Evans, and J. C. Green (2006), Observations and modeling of energetic electron dynamics during the October 2001 storm, *J. Geophys. Res.*, **111**, A11S02, doi:10.1029/2005JA011351.
- O'Brien, T. P., M. D. Looper, and J. B. Blake (2004), Quantification of relativistic electron microburst losses during the GEM storms, *Geophys. Res. Lett.*, **31**, L04802, doi:10.1029/2003GL018621.
- Orlova, K. G., and Y. Y. Shprits (2011), On the bounce-averaged of scattering rates and the calculations of bounce period, *Phys. Plasmas*, **18**, 092,904, doi:10.1063/1.3638137.
- Orlova, K. G., Y. Y. Shprits, and B. Ni (2012), Bounce-averaged diffusion coefficients due to resonant interaction of the outer radiation belt electrons with oblique chorus waves computed in a realistic magnetic field model, *J. Geophys. Res.*, **117**, A07209, doi:10.1029/2012JA017591.
- Ozeke, L. G., I. R. Mann, K. R. Murphy, I. J. Rae, D. K. Milling, S. R. Elkington, A. A. Chan, and H. J. Singer (2012), ULF wave derived radiation belt radial diffusion coefficients, *J. Geophys. Res.*, **117**, A04222, doi:10.1029/2011JA017463.
- Reeves, G. D., K. L. McAdams, R. H. W. Friedel, and T. P. O'Brien (2003), Acceleration and loss of relativistic electrons during geomagnetic storms, *Geophys. Res. Lett.*, **30**(10), 1529, doi:10.1029/2002GL016513.
- Reeves, G. D., Y. Chen, G. S. Cunningham, R. W. H. Friedel, M. G. Henderson, V. K. Jordanova, J. Koller, S. K. Morley, M. F. Thomsen, and S. Zaharia (2012), Dynamic Radiation Environment Assimilation Model: DREAM, *Space Weather*, **10**, S03006, doi:10.1029/2011SW000729.
- Roederer, J. G. (1970), *Dynamics of Geomagnetically Trapped Radiation*, Springer, New York.
- Schulz, M., and L. Lanzerotti (1974), *Particle Diffusion in the Radiation Belts*, Springer, New York.
- Selesnick, R. S., and J. B. Blake (2000), On the source location of radiation belt relativistic electrons, *J. Geophys. Res.*, **105**(A2), 2607–2624, doi:10.1029/1999JA900445.
- Sheeley, B., M. Moldwin, H. Rassoul, and R. Anderson (2001), An empirical plasmasphere and trough density model: CRRES observations, *J. Geophys. Res.*, **106**, 25,631–25,641, doi:10.1029/2000JA000286.
- Shprits, Y. Y., R. M. Thorne, G. D. Reeves, and R. Friedel (2005), Radial diffusion modeling with empirical lifetimes: Comparison with CRRES observations, *Ann. Geophys.*, **23**, 1467–1471.
- Shprits, Y. Y., R. M. Thorne, R. B. Horne, S. A. Glauert, M. Cartwright, C. T. Russell, D. N. Baker, and S. G. Kanekal (2006), Acceleration mechanism responsible for the formation of the new radiation belt during the 2003 Halloween solar storm, *Geophys. Res. Lett.*, **33**, L05104, doi:10.1029/2005GL024256.
- Shprits, Y. Y., N. P. Meredith, and R. M. Thorne (2007), Parameterization of radiation belt electron loss timescales due to interactions with chorus waves, *Geophys. Res. Lett.*, **34**, L11110, doi:10.1029/2006GL029050.
- Su, Z., H. Zheng, and S. Wang (2010), Three-dimensional simulation of energetic outer zone electron dynamics due to wave-particle interaction and azimuthal advection, *J. Geophys. Res.*, **115**, A06203, doi:10.1029/2009JA014980.
- Su, Z., F. Xiao, H. Zheng, and S. Wang (2011), CRRES observation and STEERB simulation of the 9 October 1990 electron radiation belt dropout event, *Geophys. Res. Lett.*, **38**, L06106, doi:10.1029/2011GL046873.
- Subbotin, D. A., Y. Y. Shprits, and B. Ni (2011), Long-term radiation belt simulation with the VERB 3-D code: Comparison with CRRES observations, *J. Geophys. Res.*, **116**, A12210, doi:10.1029/2011JA017019.
- Summers, D. (2005), Quasi-linear diffusion coefficients for field-aligned electromagnetic waves with applications to the magnetosphere, *J. Geophys. Res.*, **110**, A08213, doi:10.1029/2005JA011159.
- Summers, D., and R. M. Thorne (2003), Relativistic electron pitch-angle scattering by electromagnetic ion cyclotron waves during geomagnetic storms, *J. Geophys. Res.*, **108**(A4), 1143, doi:10.1029/2002JA009489.
- Summers, D., R. M. Thorne, and F. L. Xiao (1998), Relativistic theory of wave-particle resonant diffusion with application to electron acceleration in the magnetosphere, *J. Geophys. Res.*, **103**(A9), 20,487–20,500.
- Tao, X., J. Bortnik, J. M. Albert, K. Liu, and R. M. Thorne (2011), Comparison of quasilinear diffusion coefficients for parallel propagating whistler mode waves with test particle simulations, *Geophys. Res. Lett.*, **38**, L06105, doi:10.1029/2011GL046787.
- Tao, X., J. Bortnik, J. M. Albert, and R. M. Thorne (2012), Comparison of bounce-averaged quasi-linear diffusion coefficients for parallel propagating whistler mode waves with test particle simulations, *J. Geophys. Res.*, **117**, A10205, doi:10.1029/2012JA017931.
- Temerin, M., I. Roth, M. K. Hudson, and J. R. Wygant (1994), ‘New Paradigm for the Transport and Energization of Radiation Belt Particles’, *AGU, Eos*, 538.
- Thorne, R. M., T. P. O'Brien, Y. Y. Shprits, D. Summers, and R. B. Horne (2005), Timescale for MeV electron microburst loss during geomagnetic storms, *J. Geophys. Res.*, **110**, A09202, doi:10.1029/2004JA010882.
- Tsyganenko, N. A. (1989), A magnetospheric magnetic field model with a warped tail current sheet, *Planet. Space Sci.*, **37**, 5–20.
- Tu, W., X. Li, Y. Chen, G. D. Reeves, and M. Temerin (2009), Storm-dependent radiation belt electron dynamics, *J. Geophys. Res.*, **114**, A02217, doi:10.1029/2008JA013480.
- Tu, W., R. Selesnick, X. Li, and M. Looper (2010), Quantification of the precipitation loss of radiation belt electrons observed by SAMPEX, *J. Geophys. Res.*, **115**, A07210, doi:10.1029/2009JA014949.
- Tu, W., S. R. Elkington, X. Li, W. Liu, and J. Bonnell (2012), Quantifying radial diffusion coefficients of radiation belt electrons based on global MHD simulation and spacecraft measurements, *J. Geophys. Res.*, **117**, A10210, doi:10.1029/2012JA017901.
- Ukhorskiy, A. Y., K. Takahashi, B. J. Anderson, and H. Korth (2005), Impact of toroidal ULF waves on the outer radiation belt electrons, *J. Geophys. Res.*, **110**, A10202, doi:10.1029/2005JA011017.
- Vampola, A., J. Osborn, and B. Johnson (1992), CRRES magnetic electron spectrometer AFGL-701-5A (MEA), *J. Spacecr. Rockets*, **29**(4), 592–595, doi:10.2514/3.25504.
- Wentworth, R. C., W. M. MacDonald, and S. F. Singer (1959), Lifetimes of trapped radiation belt particles determined by Coulomb scattering, *Phys. Fluids*, **2**, 499.